THE JOURNAL OF PHYSICAL CHEMISTRY C

Article

Cite This: J. Phys. Chem. C 2018, 122, 9292−9301

pubs.acs.org/JPCC

# Reversal in the Lattice Contraction of $\alpha$-$Fe_2O_3$ Nanoparticles

Monika Sharma,[†] Sevi Murugavel,*[,†] Dinesh Kumar Shukla,[‡] and Frank M. F. De Groot[§]

[†]Department of Physics and Astrophysics, University of Delhi, Delhi 110 007, India

[‡]UGC-DAE Consortium for Scientific Research, University Campus, Khandwa Road, Indore 452 001, India

[§]Inorganic Chemistry & Catalysis, Debye Institute for Nanomaterials Science, Utrecht University, Universiteitsweg 99, 3584 CG, Utrecht, The Netherlands

Supporting Information

**ABSTRACT:** We report the discovery of size-dependent lattice contractions and elongations in the nanoscale hematite ($\alpha$-$Fe_2O_3$) structure revealed by high-resolution X-ray diffraction analysis and spectroscopic measurements. The observed lattice modification effects are classified into two different regions with the crystallite size (CS) with a threshold anomaly at ≈30 nm. In addition to the commonly observed lattice expansion in ionic solids, we report the discovery of lattice contraction at the nanoscale level (<30 nm CS). The consequences of anomalous structural behavior with the CS are reflected in the electronic and vibrational properties of the hematite structure. The characteristic behavior in structural and electronic properties of the hematite structure is closely linked with changes in the bonding character, which shows strong dependence on the CS. We suggest that the lattice expansion is caused by weaker hybridization of $e_g$ states, whereas at the nanoscale regime the increased level of Fe 4sp−O 2p hybridization leads to less oxygen 2p to hybridize with the 3d-states, implying an increased level of covalency and reduction in the unit cell parameters. Furthermore, the change in the bonding characteristics leads to the enhanced polaronic conductivity of 4 orders of magnitude at the nanoscale level, which is highly beneficial for the unique structural advantage of the iron oxide and its derived compounds.

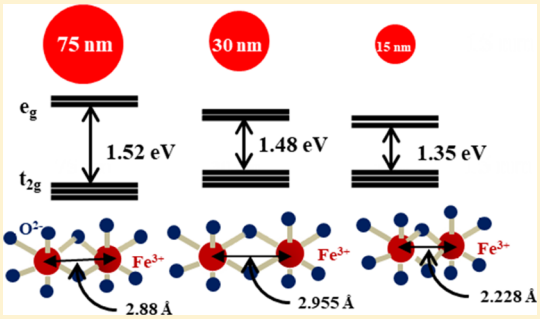


## INTRODUCTION

Iron oxides constitute an important class of minerals that is pervasive in nature. The most important geo- and biochemical redox reactions are lined either with formation or transformation of iron oxides from one state to another by charge transfer (CT) processes, which cycle the iron between its two oxidation states.[1−5] Recently, much attention has been devoted to synthesis and characterization of hematite nanostructures toward their applications in photoelectrochemical cells for water splitting, gas sensors, magnetic recording media, and as anode materials for lithium-ion batteries.[6−9] Among the various forms of iron oxides, the bulk hematite structure ($\alpha$-$Fe_2O_3$) is an n-type semiconductor with an energy gap of ≈1.9 eV at room temperature and is the most thermodynamically stable phase. Because of its semiconducting nature, the nanosized hematite particle has great advantage of tuning its physical and chemical properties. Its applicability as a better anode material for lithium-ion batteries merits in terms of its nontoxicity, low cost, and high capacity. In comparison with the conventional graphite anode material for lithium-ion batteries, $\alpha$-$Fe_2O_3$ exhibits high capacity (1005 mA h $g^{-1}$), which is 2.7 times higher than that of graphite. In recent years, various morphologies of $Fe_2O_3$ such as monodisperse nanocrystals, nanotubes, hollow structures, nanowires, and free-standing nanomembranes are demonstrated to be highly advantageous to improve the performance of Li-ion batteries.[9] However, the commercialization of $\alpha$-$Fe_2O_3$ as the anode material for energy storage devices is still limited by the poor capacity retention with short life because of the volume expansion/contraction upon repeated cycling and low polaronic conductivity. Thus, there are still great challenges to achieve extended cycle life and high rate capability with adequate reversible capacity for high-power energy storage devices.

In spite of the growing importance of nanosized $\alpha$-$Fe_2O_3$ structure in practical applications, the fundamental understanding of the intrinsic defects in hematite structure is not clear yet. The electronic properties are controlled by the defects present in the hematite structure because the concentration and type of the defect decide the charge transport mechanism. In particular, the oxygen vacancies are expected to be the dominant one and act as shallow donor dopants in hematite, that is, energy levels close to the conduction band minimum.[10] The creation of each oxygen vacancy leads to two excess electrons and forms polaronic sites ($Fe^{2+}$), and this would increase the carrier (polaron) concentration and therefore the overall electrical conductivity enhancement. An early experimental investigation on nonstoichiometric $Fe_2O_{3-\delta}$ revealed its partial pressure dependency on the electrical properties.[11]

Received: January 17, 2018
Revised: April 11, 2018
Published: April 11, 2018






DOI: 10.1021/acs.jpcc.8b00550
J. Phys. Chem. C 2018, 122, 9292−9301

There have been few computational investigations on the defect properties of $\alpha$-$Fe_2O_3$ using classical approaches.[12] More importantly, these studies reveal that the changes in the oxygen vacancy concentrations can lead to structural phase transition from hematite to maghemite ($\gamma$-$Fe_2O_3$).[13] Therefore, by considering the complex nature of multivalent oxides like $\alpha$-$Fe_2O_3$, a detailed investigation at the ab initio level is highly desirable. In this context, the importance of defect states in the hematite structure becomes more relevant in nanosized $\alpha$-$Fe_2O_3$ than the bulk one because of the surface energy kinetics.

Another interesting aspect of transition metal oxides (TMOs) is the size-dependent lattice anomaly with the reduction of the particle size below a micron meter scale. More commonly, lattice parameters are the basic quantity which characterizes any crystalline solid, and thus, their variation directly affects the physical properties. The size-dependent lattice expansion has been observed in various TMO nanoparticles,[14,15] while lattice contraction prevails for pure metal nanoparticles.[16,17] Though the size-induced lattice changes are observed in a wide range of oxides, the fundamental origin has been the subject of debate.[18] To understand the various intriguing properties of the $\alpha$-$Fe_2O_3$ structure with the crystallite size (CS), we have carried out detailed and systematic investigations at the atomic level.

In this contribution, we report for the first time, combined physical and structural properties of the $\alpha$-$Fe_2O_3$ structure with different CSs. In this context, we have synthesized the various CSs of $\alpha$-$Fe_2O_3$ ranging from bulk (75 nm) to 15 nm by adopting the typical sol−gel technique. The phase confirmation of different CSs of $\alpha$-$Fe_2O_3$ was established by using the high-resolution X-ray diffraction (XRD) analysis along with the vibrational spectroscopic techniques like Raman and Fourier transform infrared (FTIR) spectroscopy. More quantitatively, the analysis of the XRD pattern by the Rietveld method yielded systematic changes in the unit cell parameters with the CS. It is worthwhile to mention that the lower limit of the CS has been restricted to 15 nm, because below this size the hematite structure has transformed into maghemite ($\gamma$-$Fe_2O_3$).[13] On the basis of the obtained results, we classify $\alpha$-$Fe_2O_3$ into two different regions with respect to the CS, where it shows the threshold anomaly in different physical, electronic, and structural properties. Size-dependent lattice expansion of the hematite structure is observed between bulk (75 nm)−30 nm CS (named as region-II). On the other hand, below 30 nm we observe lattice contraction continuously up to 15 nm CS (named as region-I), which brings many beneficial properties for different applications. The observed anomalous behavior of $\alpha$-$Fe_2O_3$ with the CS is closely related to changes in the hybridization between the metal and ligand orbital monitored by the X-ray absorption spectroscopy (XAS) technique. The anomalous changes in the structural properties are reflected in the electronic properties of the hematite structure, where we find polaronic conductivity enhancement of 4 orders of magnitude at the nanoscale level.

## EXPERIMENTAL SECTION

Different crystallite sized $\alpha$-$Fe_2O_3$ has been synthesized by using the sol−gel procedure. We used hydrated iron nitrate $Fe(NO_3)_3{\cdot}9H_2O$ as the precursor solution, and it was gelated by using monohydrated citric acid (Aldrich 98%) solution (0.05 M) as ligand molecules and singly distilled water as the solvent. The iron precursor solution was added into the citric acid solution dropwise with vigorous stirring at 70 °C until the gel was formed. To obtain monodispersed crystallites of different sizes, we have varied molar concentrations of citric acid and iron nitrate. Subsequently, the dried gel was annealed at 550 °C, yielding different crystallite sized $\alpha$-$Fe_2O_3$ structures. We attempted to prepare CS of below 15 nm but ended up in the maghemite ($\gamma$-$Fe_2O_3$) phase. Therefore, the present work deals only with the hematite ($\alpha$-$Fe_2O_3$) structure, with the CS ranging between 75 and 15 nm.

XRD measurements were performed on a Bruker D8 diffractometer using a Cu K$\alpha$ source, ($\lambda$ = 1.5441 Å) arrayed with a scintillation detector operating at 40 kV to 40 mA with the 2$\theta$ scan range of 15°−70° providing the step size 0.02°. The crystal structures were then refined with the help of the Rietveld refinements method by using TOPAS software, starting the refinement with the initial cell parameters reported in the JCPDS data (File no. -01-079-007) and literature. The profiles were refined to $R_{wp}$ < 3.4 and special efforts were made to obtain unit cell parameters within the error bars of ±0.001°. The crystal structure of hematite is same as that of corundum $Al_2O_3$, which can be described as the rhombohedral unit cell with the space group $R\bar{3}c$ and Fe ions occupy two-thirds of octahedral interstitial sites. Each unit cell consists of 6 $Fe_2O_3$ formula units including 12 Fe atoms and 18 O atoms. The fitting was done for the entire data set collected in the 2$\theta$ range from 15° to 70° and by starting with the Le Bail fit, in which nominal cell parameters were inserted without providing atomic coordinates and occupancy factor. After Le Bail fit converged to a satisfactory limit, proper Rietveld analysis was started by providing all atomic parameters along with the occupancy factors. However, during the first stage, all parameters were kept close to those reported, and all occupancies were constrained to the ideal value of unity.

To gain further insight into the site occupancies and the new findings in the unit cell parameters, careful analysis on the Rietveld data has been carried out. For larger CS, in the initial stages of refinement, Fe occupancy was constrained to its nominal value (1) and varied O occupancy converged close to one. On the other hand, for the CSs lower than 50 nm, a substantial improvement in the fit was obtained only when O partial occupancy was left to vary without constraints, resulting in a partial occupancy of 0.952 for O atoms in the case of 15 nm CS. It should be emphasized that the occupancy of O atoms monotonically decreased to 0.952 from its nominal value. Subsequently, Fe and O occupancies were allowed to vary free of constraints, that is, equal to one, and the value obtained in each stage was used as starting parameters for further refinements. An improvement in the fit was observed when simultaneous presence of Fe and O was allowed in their sites, whereas no convergence was seen when instantaneous presence of O in Fe site or vice-versa. Finally, O occupancy was allowed to vary simultaneously with Fe occupancy. In all the cases, temperature factors were kept to isotropic mode. The lattice parameters, reliability factors, and atomic coordinates obtained are listed in Table S2 for 75 nm CS.

The morphological nature of the obtained nanocrystals has been investigated by using transmission electron microscopy. Carbon-coated formvar copper grids were dipped in nanoparticle dispersions and imaged by the Tecnai high resolution transmission electron microscope (HRTEM; TECNAI $G^2$ T30 U-TWIN) attached with a double slit holder (±70°) under an accelerating voltage of 300 kV. The images have been recorded by using a CCD camera (Gatan) with the resolution of 0.19 nm. Analysis of the TEM images and calculation of lattice


DOI: 10.1021/acs.jpcc.8b00550
J. Phys. Chem. C 2018, 122, 9292−9301

spacing has been calculated by using the Digital Micrograph software (Gatan). The particle size and surface morphology of all the samples were measured by field emission scanning electron microscopy (FESEM; GeminiSEM 500 by ZEISS). The images have been recorded with the same magnification choosing the different area over the grid. After recording the images, the particle sizes have been analyzed with the help of ImageJ software which enables one to enhance the image contrast and sharpening of the images. After calibrating the scale according to the image magnification, the size of each particle has been measured and listed in the form of table. Afterward, the histogram was made with the listed values in the table followed by peak fitting which results into the Gaussian distribution.

XAS on Fe L-edge and O K-edges was performed at the SXAS beamline (BL-01) of the INDUS 2 synchrotron source at RRCAT, Indore, India, operating at 2.5 GeV energy with a maximum storage current of 150 mA. The room temperature XAS data were collected in total electron yield (TEY) mode under ultra-high vacuum ($10^{-10}$ Torr) conditions and normalized with respect to incident photon flux. Grating with 1500 grooves per mm with the entrance and exit slit size of 1000 and 100 $\mu$m was used for collecting the spectra in the energy ranges of 500−580 eV for O 1s and 700−740 eV for Fe L-edge. The energy resolution was 0.2 and 0.3 eV for O 1s and Fe L-edge, respectively. Pre-edge and postedge correction of normalized XAS data was performed using Athena software.

The FTIR spectra were recorded with Thermo Scientific (NICOLET 380) system in transmittance mode and on pellets made by KBr and sample with weight ratio of 1:100 (sample to KBr). In Figure S7, we illustrate the measured FTIR spectra of the $\alpha$-$Fe_2O_3$ with different CSs in the range of 400−1000 $cm^{-1}$, where the characteristic absorption band intensity and position shows pronounced change with size. The room temperature Raman spectra were recorded in the 180° back scattering geometry, using a 785 nm excitation of air-cooled argon ion laser (Renishaw InVia Reflex Micro Raman Spectrometer). Spectral resolution of the instrument was better than 1 $cm^{-1}$ and the incident power was fixed to 10 mW for all the samples.

Diffuse reflectance spectra (DRS) of all the samples with different particle sizes were recorded using a PerkinElmer UV−vis spectrophotometer (Lambda-65), the spectral resolution of the instrument is around 0.5 nm. In the DRS, ethanol was used as the reference sample, and then, the samples were mixed with ethanol and recorded the absorbance spectra covering the full range from 200 to 1100 nm. Optical absorption spectroscopy measurements on the hematite structure with different CSs reveal the electronic structure, and it again supports the observed anomalous polaronic conductivity behavior with the CS. The Tauc plot has been derived from the DRS, and then, the optical band gap of the corresponding crystallite structure has been estimated.

Broad band impedance measurements were performed on circular disc-shaped pellets by using a Novocontrol $\alpha$-S high-resolution dielectric analyzer. The $\alpha$-$Fe_2O_3$ powder was first pressed into pellets of 13 mm diameter and thickness of 1 mm by means of uniaxial press (4 ton). Ionically, blocking electrodes were made by sputtering silver/gold layers on both sides of the compact pellet. The ac impedance measurements were made in a frequency range from 10 mHz to 1 MHz, at temperatures between 273 and 573 K. The dc conductivity has been extracted by fitting the frequency-dependent conductivity spectra by using the Jonscher power law relation. In the present work, we discuss only the size-dependent dc conductivity at 313 K and explore the origin of polaronic conductivity enhancement and its interdependence on the optical band gap.

## RESULTS AND DISCUSSION

The crystallographic structures of the obtained powdered samples with different CSs were analyzed by the XRD method. The obtained diffraction patterns are well-indexed to the rhombohedral hematite ($\alpha$-$Fe_2O_3$) structure (JCPDS file no: 01-079-007), and no other parasitic phases ($\gamma$, $\beta$, $\delta$-$Fe_2O_3$ or iron oxide hydroxide) has been detected in all the CSs as shown in Figure S1 (see the Supporting Information). The average CSs of all the samples have been estimated by using the Williamson Hall relation[19] given by

$$\beta \cos\theta = \frac{k\gamma}{D} + 4\varepsilon \sin\theta \quad (1)$$

where $\beta \cos(\theta)$ is plotted against $\sin(\theta)$, the intercept of the straight line would provide the CS of the particular sample, and the slope will be associated with the lattice strain. After removing the contribution of strain in the peak broadening, the CS of each sample has been calculated and it was found to be in the range between 75 and 15 nm. The lowest CS has been limited to 15 nm because below this size we observed emergence of the maghemite ($\gamma$-$Fe_2O_3$) phase, which is in agreement with earlier studies.[13,20] Additionally, we have confirmed the CS distribution of individual $\alpha$-$Fe_2O_3$ particles in the present investigation by using the HRTEM shown in Figure S2 (see the Supporting Information). An estimated average CS and lattice spacing of all the samples in the present investigation by XRD and HRTEM are listed in Table S1. It is interesting to note that there is good agreement between estimated values by XRD and HRTEM. Furthermore, we have carried out FESEM investigations to reveal the surface morphology and particle size distribution. The surface morphology by FESEM reveals that the particles are spherical in shape and uniformly dispersed as shown in Figure S3 (see the Supporting Information). The particle size analysis indicates that the lower-sized sample possesses relatively narrow-sized distribution than the larger-particle-sized sample.

The crystal structure of hematite is same as that of corundum $Al_2O_3$, which can be described as the rhombohedral unit cell with the space group $R\bar{3}c$, and Fe ions occupy two-thirds of octahedral interstitial sites. An each unit cell consists of 6 $Fe_2O_3$ formula units including 12 Fe atoms and 18 O atoms. Furthermore, the crystal structure was refined using the Rietveld-refinement analysis, they are completely indexed to the space group of $R\bar{3}c$ as shown in Figure S4 (see the Supporting Information), and it has resulted with lattice constants of $a = b = 5.036(1)$ (Å), $c = 13.751(3)$ (Å) and $V = 302.192(11)$ (Å$^3$) for the bulk CS (75 nm).[21,22] The profiles were refined to $R_{wp} < 3.4$, and special efforts were made to obtain unit cell parameters within the error bars of ±0.001°. The structural parameters obtained from the Rietveld refinement for representative 75 and 15 nm CS are tabulated in Table S2a,b (see the Supporting Information). Similarly, we extracted the lattice parameters of all the CSs using the Rietveld analysis and depicted in Figure 1. As shown in Figure 1a, the CS reduction leads to the expansion of lattice constant and unit cell volume until 30 nm. The present results are in agreement with earlier observation on $\alpha$-$Fe_2O_3$ bulk and nanocrystals.[14,23] Remarkably, with the further reduction in size (<30 nm), the lattice constants and cell volume decrease significantly and the



DOI: 10.1021/acs.jpcc.8b00550
J. Phys. Chem. C 2018, 122, 9292−9301

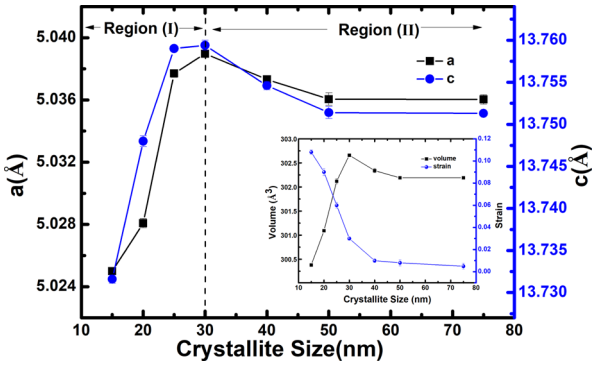


**Figure 1.** Unit cell parameters as a function of CS for $\alpha$-$Fe_2O_3$. (a) Variation of unit cell parameters with CS for $\alpha$-$Fe_2O_3$ obtained by Rietveld refinements. These values are refined with the $R\bar{3}c$ space group. It is also of interest that the unit cell expansion followed by contraction is isotropic, where *a* and *c* show the similar variation with the CS. The variation of unit cell parameters with the CS is divided into two regions such as expansion and contraction. The inset shows the variations of unit cell volume and strain with the CS are estimated from the Le Bail profile fitting. The line connecting the points is drawn as a guide to the eye.

obtained value for 15 nm CS is much lower than that of the bulk value.

More commonly, the increase in the crystallographic cell volume has been observed in the hematite structure as well as other TMOs with the reduction of the CS.[22] To our knowledge, there is only a report in the literature on NiO which experiences the similar behavior, that is, increase and then decrease in unit cell parameters with the reduction of the particle size.[24] However, the threshold anomaly in NiO is different from the hematite structure, and the authors do not provide any justifications for the observed size-dependent variations in the lattice constants. In this present work, we observe 0.15% expansion followed by 0.5% contraction in the cell volume with respect to the macroscopic crystal structure of hematite shown in the inset of Figure 1. Again, the percentage of volume expansion (0.15%) is consistent with the earlier reports on hematite nanocrystals.[23] However, reduction of the CS below 30 nm leads to the contraction in unit cell parameters, which should be different origin from the initial lattice expansion. To gain further insight into the site occupancies and the new findings in the unit cell parameters, careful analysis on the Rietveld data has been carried out. For larger CS, in the initial stages of refinement, Fe occupancy was constrained to its nominal value (1) and varied O occupancy converged close to one. On the other hand, for the CSs lower than 50 nm, a substantial improvement in the fit was obtained only when O partial occupancy was left to vary without constraints, resulting in a partial occupancy of 0.952 for O atoms in the case of 15 nm CS. It should be emphasized that the occupancy of O atoms monotonically decreased to 0.952 from its nominal value. We have also estimated the resulting lattice strain with the reduction of the CS from the Rietveld analysis, which shows the substantial enhancement below 30 nm CS as illustrated in the inset of Figure 1. The observed anomalous size-dependent variation of lattice constants and cell volume are an intrinsic property of hematite crystals caused by the change in the molecular structure with the reduction of CS. Thus, it is highly necessary to understand the nature of atoms and their surrounding environments which determines valance state, hybridization, and covalency effects because these fundamental quantities determine the unit cell parameters as well as other physical properties. In the following section, we provide direct evidence for the changes in the local bonding character and its close connection with the observed unit cell parameters.

To obtain appropriate microstructural information, XAS measurements were carried out at the SXAS beamline (BL-01) of the INDUS 2 synchrotron source at RRCAT, Indore. Figure S5 shows the normalized Fe $L_{2,3}$ edges related to the excitation of a 2p core electron of hematite with different CSs recorded at room temperature. Both these $L_3$ and $L_2$ edges are further divided into $t_{2g}$ and $e_g$ levels because of crystal-field splittings and atomic multiplet effects.[25] A careful observation of the $L_3$ edge shows that the intensity of the $t_{2g}$ level is lower than the $e_g$ level and their difference in the peak maximum is related to the crystal-field splitting (10Dq) energy. To gain further insights, we used a freeware interface version of the multiplet code available under the name of charge transfer multiplets for XAS (CTM4XAS).[26] By using the CTM4XAS, we have simulated the Fe $L_{3,2}$ edges and compared the results with the experimental spectra as shown in Figure S6 (see the Supporting Information). For the larger CS (75 nm), the spectral shape, peak position, and 10Dq are similar to those reported in the literature on the bulk hematite structure by assuming to be high spin $^6A_1$ ground state, dominated by the $[t_{2g}]^3$ $[e_g]^2$ configuration.[27] Though the spectral features are similar in the entire range CS, the value of 10Dq shows pronounced size dependence, indicating that the 3d electron density become dependent on the CS and is shown in Figure S7 (see the Supporting Information).

In Figure 2, we depict the oxygen 1s XAS spectra of $\alpha$-$Fe_2O_3$ with various CSs, where significant changes in the intensity of pre-edge region (530−535 eV) and postedge region (536−546 eV) have been observed. In Fe-based oxides, the pre-edge spectral features are associated with the number of unoccupied 3d metal states which are hybridized with the O 2p states. On the other hand, the features in the postedge region are O 1s

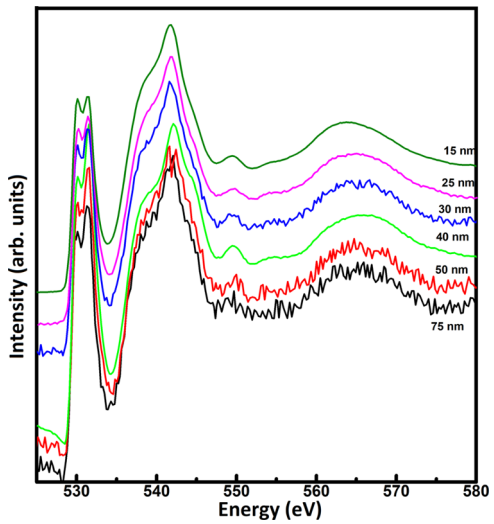


**Figure 2.** Soft X-ray absorption spectrum of O 1s for different CSs of $\alpha$-$Fe_2O_3$. Oxygen 1s X-ray absorption spectra of $\alpha$-$Fe_2O_3$ recorded in TEY for various CSs. The doublet peak centered around 530 eV is assigned to the oxygen p character in the transition metal 3d band. The broader band centered around 540 eV corresponds to the oxygen p character in the metal 4s and 4p bands.



DOI: 10.1021/acs.jpcc.8b00550
J. Phys. Chem. C 2018, 122, 9292−9301

electron transitions into O 2p states which are hybridized with Fe (4s, 4p) states.[28,29] The changes in the O 1s XAS spectral intensity with the CS are larger than that of the Fe 2p XAS spectral intensity. Remarkably, the intensity of the $t_{2g}$ and $e_g$ peaks in pre-edge and postedge region varies with the CS, where the intensities of spectral features are related to the spin states and/or the number of electrons in the d orbitals.[28] In TMOs, the ratio $t_{2g}/e_g$ is expected to be 3:2 for $d^5$ and 0:2 for $d^8$ electrons provided if the covalency is the same of the $t_{2g}$ and $e_g$ electrons. However, the experimental studies on various TMOs reveal that the hybridization of the $e_g$ states is stronger than the $t_{2g}$ state implying that the ratio become 1:1 instead of 3:2 because of increased covalence of $e_g$ electrons. Therefore, the intensity ratio of these spectral features provides information about the nature of ions involved in the hybridization process or the intensity ratio is equivalent to the amount of covalent mixing between iron and oxygen. To proceed for a quantitative determination area under the $t_{2g}$ and $e_g$ peak, it is necessary to use the deconvolution procedure with the aim of separating individual contributions. In Figure 3, we

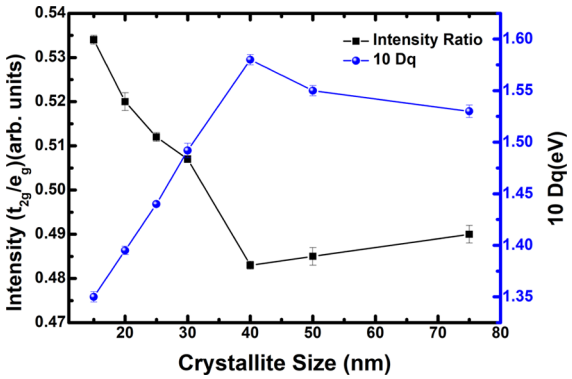


**Figure 3.** CS-dependent intensity ratio of the $t_{2g}$ and $e_g$ peaks (left *y*-axis) and the difference 10Dq (right *y*-axis) calculated from O 1s XAS spectra of $\alpha$-$Fe_2O_3$. The intensity ratio is equivalent to the amount of covalent mixing between oxygen 2p and metal 3d sates. Under the influence of an octahedral ligand field, the d orbitals split into two groups of different energy ($t_{2g}$ and $e_g$) levels and their difference is denoted as 10Dq or crystal-field splitting energy ($\Delta_o$). The line connecting the points is drawn as a guide to the eye.

show the estimated intensity ratio (pre-edge region) of $\alpha$-$Fe_2O_3$ with different CSs, where the ratio is found to be less than one in all the CSs. Interestingly, the CS-dependent intensity ratio shows anomalous behavior, where it decreases with the reduction of the CS from the bulk and then it increases sharply below 40 nm CS. At first, the intensity ratio of bulk $\alpha$-$Fe_2O_3$ is different from that reported for the high spin state of $Fe^{3+}$ ions ($d^5$), which suggests that the involvement of oxygen 2p and metal 3d hybridization. With the reduction of CS (region-II) from its bulk value, it is clear from the O 1s XAS spectra that the intensity of the $e_g$ peak increases from bulk (75 nm) up to 40 nm. In TMOs with octahedral complexes, the metal $e_g$ orbitals ($d_{x^2-y^2}$ and $d_{z^2}$) are directed toward the oxygen atoms and overlap strongly with the oxygen 2p orbitals. The decrease in the intensity ratio ($t_{2g}/e_g$) implies the reduction in the covalence by the lattice elongation, that is, the hybridization of $e_g$ states becomes weaker (region-II). On the other hand, for below 40 nm CS the intensity ratio of the O 1s XAS spectra shows the distinct behavior, where the 3d $t_{2g}$ contribution becomes dominant at the expanse of the $e_g$ level. In addition to the pre-edge region, it is worthwhile to note the changes in the second component intensity (energy near 540−545 eV). The intensity at the postedge region is related to the O 2p character in bands hybridized predominantly with the transition metal 4sp character. Hence, the main bonding between iron and oxygen is 4s and 4p orbitals of iron and the oxygen 2p orbitals at lower CSs. It is interesting to note that the increased level of Fe 4sp−O 2p hybridization leads to the less oxygen 2p to hybridize with the 3d-states, implying increased level of covalency and reduction in the unit cell parameters.

For the TMOs with octahedral symmetry, if the degeneracy of the d orbital is lifted then it leads to the splitting of d orbital into two groups with different energies ($t_{2g}$ and $e_g$) levels. The difference in energy between $t_{2g}$ and $e_g$ levels is called as crystal-field splitting energy (10Dq or $\Delta_o$), and it strongly depends on the nature of the ligand and charge state of the metal ion. In Figure 3, we illustrate the extracted 10Dq values from the O 1s XAS study on the hematite structure with different CSs. For the bulk crystallite $\alpha$-$Fe_2O_3$ structure, the value of 10Dq is found to be 1.53, similar to the earlier reported value in the literature.[27] The CS-dependent variation of 10Dq shows the opposite behavior to the intensity ratio ($t_{2g}/e_g$), where it complements with each other. With the reduction in the CS, the 10Dq value increases (region-II), and it represents the enhancement in the splitting because of the destabilization of the $e_g$ orbitals, where the charge is transferred from the ligand to the metal d level. We find an identical value of 10Dq from the oxygen K edge and the metal L-edge (figure S6 see the Supporting Information) and its variation with the CS implies that the core hole effect on the 10Dq value is similar.[30]

With the reduction of CS, we observe the maximum of 10Dq value at 40 nm CS, and then, it decreases drastically. However, for below 40 nm CS an increased level of hybridization leads to the reduction in the 10Dq value and in agreement with commonly observed in $d^0$ and $d^{10}$ configurations in both strong and weak ligand fields. The decrement in the 10Dq value for the smaller-sized crystallite implies the reduced oxygen content in the 3d band.[31] An enhanced level of covalency at lower CS is substantiated by the reduction in the Fe−O distance by X-ray photoelectron spectroscopy studies on epitaxial thin $\alpha$-$Fe_2O_3$ films and nanocrystals.[32] The covalence enhancement in the Fe−O bond accompanied by electron distribution variations in 3d orbitals with possible low spin configurations could be more favorable than the high spin configuration in this system. Furthermore, these magnetic phase transition is supported by the reduction in the magnetization of nanosized $\alpha$-$Fe_2O_3$ structures compared with the bulk counterpart.[33,34]

The observed size-dependent anomalous variations in the structural properties of $\alpha$-$Fe_2O_3$ discussed above are reflected in vibrational properties. In this context, we have used FTIR and Raman spectroscopy as tools to confirm the characteristic vibrational modes in the $\alpha$-$Fe_2O_3$ structure and its changes with the CS. We measured the FTIR spectra of each of the $\alpha$-$Fe_2O_3$ CS and observed changes in the characteristic absorption band intensity and position in the range of 400−1000 $cm^{-1}$ as shown in Figure S8 (see the Supporting Information). Group theoretical calculations predict that the hematite structure has six infrared active modes, out of which two polarized modes are vibrating along the *c*-axis (∥ modes) and four other modes are vibrating perpendicular to the *c*-axis (⊥ modes).[35,36] However, in the present work, the observed absorptions consist of four bands extracted by the deconvolution procedure based on the theoretical calculations. In Figure S9 (see the Supporting


DOI: 10.1021/acs.jpcc.8b00550
J. Phys. Chem. C 2018, 122, 9292−9301

Information), we illustrate the deconvoluted FTIR spectra of the hematite structure of representative 75 nm CS. The observed absorptions centered at about 470−482 ($E_u$) and 522−540 ($E_u$) $cm^{-1}$ correspond to the ⊥ modes of the Fe−O stretching vibrations. On the other hand, the vibrations between 526 and 662 ($A_{2u}$) $cm^{-1}$ are associated with the modes that have polarization ∥ to the *c*-axis. Furthermore, it has been reported in the literature that the properties of infrared optical modes of the hematite structure are size- and shape-dependent, because of the polarization change induced by an external magnetic field at the crystal surface.[37] The influence of the CS on the vibrational properties becomes noticeable by monitoring the characteristic vibrational mode and its position with the size. In this context, we considered $E_u$ mode centered at 482 $cm^{-1}$ and its position with the reduction in the CS. In Figure 4, we illustrate the CS-dependent FTIR vibrational peak

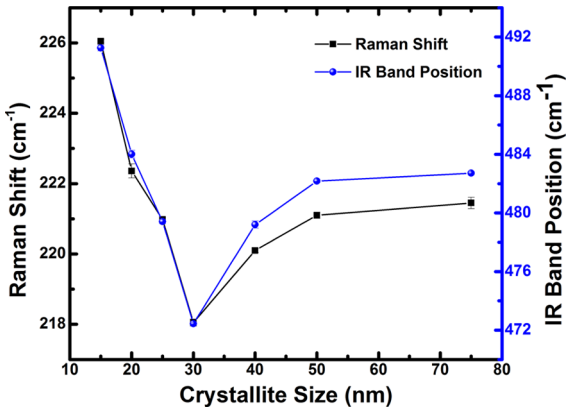


**Figure 4.** Variation of Raman band ($A_{1g}$ mode) and FTIR band ($E_u$ mode) positions with different CSs. The $A_{1g}$ mode is due to symmetrical stretching of the Fe−O bond which involves the movement of the iron ion along the *z* axis and the $E_u$ mode corresponds to the perpendicular mode of the Fe−O stretching vibrations. The line connecting the points is drawn as a guide to the eye.

maxima of 482 $cm^{-1}$, which shows the appreciable reduction in the vibrational frequency, that is, red shift up to 30 nm CS. However, for below 30 nm CS we observe that the vibrational mode shifts to a higher frequency, that is, blue shift. An earlier FTIR studies on the $\alpha$-$Fe_2O_3$ structure revealed only the red shift with the reduction of the particle size (correspondingly lattice expansion or region-II).[23,38]

Furthermore, we have characterized the hematite structure of different CSs by Raman spectroscopy and identified various Raman active modes. It is known that the hematite structure belongs to the $R\bar{3}c$ crystal space group and has seven Raman active phonon lines, namely, two $A_{1g}$ modes (221 and 498 $cm^{-1}$) and five $E_g$ modes (247, 293, 299, 412, and 613 $cm^{-1}$), respectively.[39,40] In Figure S10 (see the Supporting Information), we show the room temperature Raman spectra of the hematite structure for various CSs. In contrast to FTIR spectra, we observe that characteristic Raman active modes belong to the hematite structure and they are well-resolved and appear distinctly. Furthermore, the observed Raman bands confirm to be an intrinsic part of the hematite structure in all the CSs by the absence of any other vibrational band related to parasitic phases. It is worthwhile to mention that the distinction between bands at 293 and 299 $cm^{-1}$ is resolved only at temperatures below 100 K, and therefore, we observe only one band at room temperature.[41] In Figure 4, we depict the peak position of $A_{1g}$ mode for 75 nm vibrates at 221 $cm^{-1}$ for different CSs of the hematite structure. Remarkably, in parallel with the FTIR vibrational mode of 470 $cm^{-1}$, we observe a similar dependency on the peak position of $A_{1g}$ mode with different CSs. The $A_{1g}$ mode at around 221 $cm^{-1}$ is due to the symmetrical stretching of the Fe−O bond, which involves the movement of an iron ion along the *z* axis with the Wyckoff position (0,0,*z*). The observed size-dependent vibrational properties are intrinsic part of the hematite structure and exhibit a similar dependency on the CS. On the basis of the above experimental results, we confirm the observed behavior, that is, lattice expansion and contraction are exclusively due to the size-dependent property of the hematite structure.

As the CS decreases from bulk (75−30 nm—denoted as region-II), the hematite unit cell expands aniostropically, where the *c*-axis increases faster than the *a*-axis revealed by XRD data. Because of the unit cell volume expansion, *c*-axis directed displacements in the unit cell become more vulnerable to the size effect than the other directions and consequently exhibit the red shift. In addition, the reduction in the vibrational frequency with the decrease of the CS can be related to the force constant between the $Fe^{3+}$ and $O^{2-}$ which would become smaller because of the corresponding lattice expansion of the hematite structure. On the other hand, for the CSs below 30 nm we observe increase in the wavenumber of those vibrational frequencies discussed above, that is, blue shift corresponding to the volume contraction. According to the XRD Rietveld analysis, the crystallites in this region (30−15 nm denoted as region−I) were found to exhibit lattice contraction corresponding to the compressive strain in the hematite structure leading to the blue shift. Thus, the observed red shift (region-I) and blue shift (region-II) in the vibrational modes (perpendicular to *c*-axis) can be primarily ascribed to the size-induced lattice expansion and contraction of the hematite structure.

In addition to structural peculiarities, we also observe anomalous behavior in the electronic properties of the hematite structure with varying the CS. In the pure hematite structure, the charge transport has been described in terms of the small polaron model in which the displacement of charge carriers is coupled with distortions of nearby atoms, where the charge carrier hops from site to site.[42−45] To obtain the charge transport mechanism on a microscopic level, we used broad band conductivity spectroscopy over a wide range of frequencies and temperatures. In Figure S11 (see the Supporting Information), we illustrate the frequency-dependent conductivity spectra of $\alpha$-$Fe_2O_3$ for CS 15 nm at various temperatures. The frequency-dependent conductivity spectra are characterized by well-defined low-frequency plateaux, where the conductivity is independent of frequency, that is, polaronic dc conductivity. These plateaux allow us to determine the dc conductivity more precisely with an error of less than 1%. In Figure 5, we illustrate the estimated dc conductivity at 313 K for various CSs of the hematite structure in the present work. The obtained dc conductivity for the bulk hematite structure (75 nm) is $1.65 \times 10^{-6}$ S/cm, which is in good agreement with the earlier reported values in the literature.[42] It is interesting to note that the bulk effect prevails up to 50 nm and then the influence of size effect starts where the polaronic dc conductivity decreases with the reduction of the CS up to 30 nm with the value of $2.48 \times 10^{-9}$ S/cm. Remarkably, we find that the polaronic dc conductivity increases below 30 nm CS and it attains the value of $2.035 \times 10^{-4}$ S/cm for 15 nm CS, and


DOI: 10.1021/acs.jpcc.8b00550
J. Phys. Chem. C 2018, 122, 9292−9301

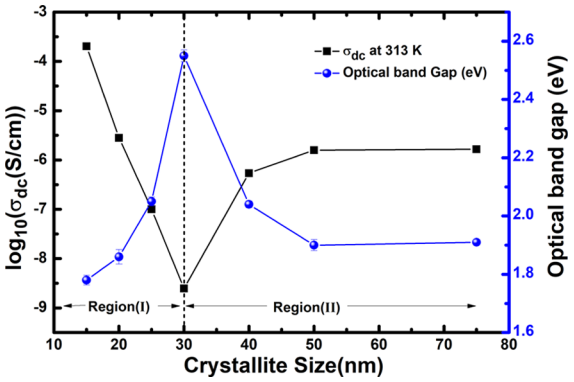


**Figure 5.** We represent the estimated polaronic conductivity, $\sigma_{dc}$, and an optical band gap, $E_g$, of hematite measured at 313 K with the CS. The $\sigma_{dc}$ has been estimated from the frequency-dependent conductivity spectra, where at low frequencies the polaronic conductivity is independent of the frequency. The optical band gap has been measured from the Tauc plot with an error in energies less than 0.05 eV. The line connecting the points is drawn as a guide to the eye. The threshold anomaly is observed at 30 nm CS in both polaronic conductivity and an optical band gap.

it is about 3 orders magnitude higher than the bulk polaronic dc conductivity. Again, we emphasize that the observed CS-dependent polaronic dc conductivity behavior is not originated from the parasitic phases and it is intrinsic part of the hematite structure. In general, the polaronic dc conductivity is determined by the several parameters such as the concentration of polarons, coupling constant (strength of the electron−phonon interaction), hopping length, hopping frequency, and activation energy. In Figure S12 (see the Supporting Information), we illustrate the temperature-dependent dc conductivity of all the CSs in the Arrhenius plot measured over a wide temperature range. Clearly, the measured dc conductivity data do not follow the simple Arrhenius behavior, rather we find two different temperature regimes corresponding to the high temperature or non-adiabatic regime and intermediate or quasi-adiabatic regime with a positive curvature as shown in the inset of Figure S12. Furthermore, we have analyzed the temperature-dependent polaronic dc conductivity using the Mott model of polaronic conduction and extracted various physical quantities associated with the hopping of charge carriers listed in Table S3 (see the Supporting Information). In the following, we discuss the origin of the anomalous behavior of dc polaronic conductivity of the hematite structure with the aid of the electronic structure revealed by various spectroscopic techniques and polaron hopping parameters (also known as Mott parameters) derived from fitting the temperature-dependent dc conductivity by using the Mott equation.

In the solids containing TMOs, an electrical conduction mechanism is described by the small polaron hopping process proposed by Mott.[43,45] In the case of the hematite structure, the active redox center is the $Fe^{3+}$ state which becomes the $Fe^{2+}$ state upon removal of oxygen atom, that is, by the presence of oxygen vacancy (source of polarons). This type of self-trapped electron corresponds to the electron polaron ($Fe^{2+}$) induced at the host $Fe^{3+}$ state. Furthermore, the electron polaron is localized at the central iron ion with the $t_{2g}$ character in the minority spin direction. Now, the ionic radius of the iron site $Fe^{2+}$ increases, which is accompanied by the polarization of the surrounding lattice. The distortion in the lattice leads to the trapping of the mobile charge carrier. The electron transfer process becomes possible only when thermal fluctuations of the lattice caused by the electronic states of the donor to coincide with the electronic states of the acceptor. The energy required to do this process is the activation energy, which must be overcome to permit the electron to hop from one site to the other.

In region-II, we observe decrease in the polaronic dc conductivity and this can be directly linked with the increase in the activation energy, electron−phonon interaction and polaron hopping length. The estimated polaron hopping length is found to increase upon reduction of the CS because of the expansion of the unit cell volume. On the other hand, at lower CSs (region-I), we find the enhancement in the polaronic dc conductivity because of the combined effect of reduction in hopping length, activation energy, and minor enhancement in the concentration of polarons. The influence of the polaron concentration becomes important only at lower CSs, where the Rietveld analysis reveal for 15 nm CS possess highest concentration of around 5% oxygen vacancy and for CSs above 30 nm, oxygen vacancy concentrations are found to be less than 1% listed in Table S3 (see the Supporting Information). The enhanced oxygen vacancy concentration at lower CSs can be understood in terms of the increased surface energy kinetics. The pronounced reduction in the hopping length at lower CS is also supported by the present XRD Rietveld analysis results and reduction in the Fe−O distance revealed by spectroscopy measurements. Furthermore, we have estimated the electron−phonon coupling constant ($\gamma$) of all the crystallites with the aid of polaron hopping energy and polaron hopping frequency suggested in the literature.[45,46] The theoretical calculations on $\gamma$ predict that if $\gamma$ is greater than 4 then it corresponds to strong coupling between electron−lattice interactions in the system, else the interactions are weak.[47] In Table S3 (see the Supporting Information), we list the estimated values $\gamma$ for the hematite structure, which vary between 5 and 10 depending on the CS. It is quite clear from the Table S3 that the reduction in the CS (region-II) leads to the enhancement in the strength of the interaction and reaches maximum for 30 nm CS, which results in the strong localization of the charge carrier. On the other hand, the strength of the interaction becomes weaker for the CSs below 30 nm and precedents to weak localization of the charge carrier. Thus, the observed anomalous polaronic dc conductivity behavior with the CS is closely related to the different microscopic quantities and they are controlled by structural distortion.

Optical absorption spectroscopy measurements on the hematite structure with different CSs reveal the electronic structure and it again supports the observed anomalous polaronic conductivity behavior with the CS. The Tauc plot has been derived from the DRS shown in Figure S13 (see the Supporting Information), and then, the optical band gap of the corresponding CS has been estimated. In Figure 5, we illustrate the obtained optical band gap of the hematite structure with varying CS, which shows the systematic trend and opposite behavior of dc polaronic conductivity. Unequivocally, we observe two distinct regions in the variation of band gap with the CS. In region-II, the estimated band gap increases with the reduction of CS and shows the maximum at 30 nm CS. On the other hand, we discovered that the band gap starts decreasing below 30 nm CS and attains the value of 1.8 eV for 15 nm CS, which is below the bulk value. The estimated band gap values for bulk hematite (75 nm) is 1.9 eV and in agreement with the


DOI: 10.1021/acs.jpcc.8b00550
J. Phys. Chem. C 2018, 122, 9292−9301

earlier reports in the literature.[48,49] There are numerous studies in the literature reporting size-dependent band gap of the hematite structure and the reported band gap values on nanoparticle/CS remain highly controversial.[50,51] The recent studies on the hematite structure reports the increase of the band gap value with decrease in the particle size,[52] and there are few other studies that report the constant value of the band gap in the entire range, that is, bulk to nanosized hematite (8 nm).[50] However, the present work reports that the observed behavior is central to the hematite structure and it varies with the CS in a reversible manner. Thus, the observed behavior of polaronic dc conductivity and optical band gap with the CS has not been reported so far to the authors' knowledge and it is an intrinsic part of the hematite structure. Though the polaronic conductivity and an optical band gap are mainly governed by the electronic structure, they are not directly interlinked like other conventional semiconductors.

It is known that bulk hematite structure has been classified as a CT magnetic insulator. In CT insulators, the top of the valance band mainly consists of oxygen 2p nonbonding orbital in addition to a set of bonding orbitals. Because of the covalency character, the orbitals corresponding to the oxygen 2p band can have a substantial contribution from the iron 3d, 4s, or 4p atomic orbitals and overlap with each other. Among the different bonding orbitals, the most relevant bonding orbital is the $e_g$ which corresponds to Fe(3d)−O (2p), $\sigma$-type interaction. The other bonding orbital is $t_{2g}$ which corresponds to the Fe(3d)−O (2p), $\pi$-type bonding interaction. On the other hand, the conduction band in the hematite structure mainly comprises the Fe 3d antibonding $e_g$ and $t_{2g}$ orbitals. Thus, the optical band gap in the hematite structure is the energy difference between the highest occupied $e_g$ (up-spin) bonding orbital and the lowest empty $t_{2g}$ (down-spin) antibonding orbital.[11]

From the reduction of the CS from the bulk value, we observe that an opening up of band gap by 0.6 eV (region-II) represents the weakening of the Fe 3d($e_g$)−O 2p hybridization and it is consistent with XAS results. Because of the increase of lattice constant, the mixing of the wave functions between Fe and O becomes less and the bandwidth of the valance band becomes small, correspondingly increasing in the band gap. On the other hand, at lower CSs (region-I) closing of the band gap takes place by 0.6 eV with respect to maximum observed at 30 nm CS. As mentioned in the previous section (XAS part), the increase in the intensity ratio ($t_{2g}/e_g$) and the decrease in crystal-field splitting energy (10Dq) indicate the enhancement in the covalency. Furthermore, we observed that the increased level of 4sp−O 2p hybridization leads to the increase of the bandwidth of the valence band, which brings the reduction in the band gap. Therefore, the present work reveals that the CS/particle size influences differently the structure and properties of TMOs at least in $\alpha$-$Fe_2O_3$.

## CONCLUSIONS

In summary, the results presented in the present work displays several important advantages featuring the nanosized hematite structure over the bulk counterpart. In addition to the lattice expansion observed in many TMOs including hematite, we have discovered the lattice contraction and discussed the underlying origin atomistically. The anomalous behavior of the hematite structure with the CS is reflected in different physical, electronic, and structural properties. The characteristic behavior of structural and electronic properties of the hematite structure is directly linked with the changes in the bonding character which shows the strong dependence with the CS. These findings demonstrate the flexibility of the hybridization (mixing) process in confined systems and suggest a strategy for both enhancement and controlling the electronic properties in different classes of materials. In addition to the relevant importance with respect to applications, such a new class of nanosized iron oxide-based compounds with their rich and fascinating crystal chemistry has become an important electrode material for the next generation of lithium-ion batteries.

## ASSOCIATED CONTENT

### Supporting Information

The Supporting Information is available free of charge on the ACS Publications website at DOI: 10.1021/acs.jpcc.8b00550.

Synthesis of $\alpha$-$Fe_2O_3$ nanocrystals, characterization technique, Rietveld refinement analysis, and polaronic hopping parameters (PDF)

## AUTHOR INFORMATION


### Corresponding Author

*E-mail: murug@physics.du.ac.in.

### ORCID

Sevi Murugavel: 0000-0002-7238-7772

Frank M. F. De Groot: 0000-0002-1340-2186


### Notes

The authors declare no competing financial interest.

## ACKNOWLEDGMENTS

One of the authors, M.S., thanks UGC for awarding the SRF fellowship. We also thank the CSIR (03(1332)/15/EMR-II) for the financial support. We acknowledge the USIC, University of Delhi, for providing facility for various characterizations during the course of work.

## REFERENCES


(1) Stumm, W.; Sulzberger, B. The Cycling of Iron in Natural Environments: Considerations Based on Laboratory Studies of Heterogeneous Redox Processes. *Geochim. Cosmochim. Acta* **1992**, *56*, 3233−3257.

(2) Bykova, E.; Dubrovinsky, L.; Dubrovinskaia, N.; Bykov, M.; McCammon, C.; Ovsyannikov, S. V.; Liermann, H.-P.; Kupenko, I.; Chumakov, A. I.; Ruffer, R.; et al. Structural Complexity of Simple $Fe_2O_3$ at High Pressures and Temperatures. *Nat. Commun.* **2016**, *7*, 10661.

(3) Vura-Weis, J.; Jiang, C.-M.; Liu, C.; Gao, H.; Lucas, J. M.; de Groot, F. M. F.; Yang, P.; Alivisatos, A. P.; Leone, S. R. Femtosecond $M_{2,3}$-edge Spectroscopy of Transition-Metal Oxides: Photoinduced Oxidation State Change in $\alpha$-$Fe_2O_3$. *J. Phys. Chem. Lett.* **2013**, *4*, 3667−3671.

(4) Garvie, L. A. J.; Zega, T. J.; Rez, P.; Buseck, P. R. Nanometer-Scale Measurements of Fe 3 +/ΣFe by Electron Energy-Loss Spectroscopy: A Cautionary Note. *Am. Mineral.* **2004**, *89*, 1610−1616.

(5) Chen, S.-Y.; Gloter, A.; Zobelli, A.; Wang, L.; Chen, C.-H.; Colliex, C. Electron Energy Loss Spectroscopy and Ab Initio Investigation of Iron Oxide Nanomaterials Grown by a Hydrothermal Process. *Phys. Rev. B: Condens. Matter Mater. Phys.* **2009**, *79*, 104103.

(6) Rioult, M.; Stanescu, D.; Fonda, E.; Barbier, A.; Magnan, H. Oxygen Vacancies Engineering of Iron Oxides Films for Solar Water Splitting. *J. Phys. Chem. C* **2016**, *120*, 7482−7490.

(7) Chen, J.; Xu, L.; Li, W.; Gou, X. $\alpha$-$Fe_2O_3$ Nanotubes in Gas Sensor and Lithium-Ion battery applications. *Adv. Mater.* **2005**, *17*, 582−586.




DOI: 10.1021/acs.jpcc.8b00550
J. Phys. Chem. C 2018, 122, 9292−9301

(8) Raj, K.; Moskowitz, R. Commercial Applications of Ferrofluids. *J. Magn. Magn. Mater.* **1990**, *85*, 233−245.
(9) Liu, X.; Si, W.; Zhang, J.; Sun, X.; Deng, J.; Baunack, S.; Oswald, S.; Liu, L.; Yan, C.; Schmidt, O. G. Free-Standing $Fe_2O_3$ Nanomembranes Enabling Ultra-Long Cycling Life and High Rate Capability for Li-Ion Batteries. *Sci. Rep.* **2014**, *4*, 7452.
(10) Yang, H.; Mi, W.; Bai, H.; Cheng, Y. Electronic and Optical Properties of New Multifunctional Materials Via Half-Substituted Hematite: First Principles Calculations. *RSC Adv.* **2012**, *2*, 10708.
(11) Lee, J.; Han, S. Thermodynamics of Native Point Defects in $\alpha$-$Fe_2O_3$: An Ab Initio Study. *Phys. Chem. Chem. Phys.* **2013**, *15*, 18906−18914.
(12) Liao, P.; Toroker, M. C.; Carter, E. A. Electron Transport in Pure and Doped Hematite. *Nano Lett.* **2011**, *11*, 1775−1781.
(13) Chernyshova, I. V.; Hochella, M. F., Jr.; Madden, A. S. Size-Dependent Structural Transformations of Hematite Nanoparticles. 1. Phase transition. *Phys. Chem. Chem. Phys.* **2007**, *9*, 1736−1750.
(14) Ayyub, P.; Palkar, V. R.; Chattopadhyay, S.; Multani, M. Effect Of Crystal Size Reduction on Lattice Symmetry and Cooperative Properties. *Phys. Rev. B: Condens. Matter Mater. Phys.* **1995**, *51*, 6135−6138.
(15) Rodenbough, P. P.; Zheng, C.; Liu, Y.; Hui, C.; Xia, Y.; Ran, Z.; Hu, Y.; Chan, S.-W. Lattice Expansion in Metal Oxide Nanoparticles: MgO, Co3O4, & Fe3O4. *J. Am. Ceram. Soc.* **2017**, *100*, 384−392.
(16) Lamber, R.; Wetjen, S.; Jaeger, N. I. Size Dependence of The Lattice Parameter of Small Palladium Particles. *Phys. Rev. B: Condens. Matter Mater. Phys.* **1995**, *51*, 10968−10971.
(17) Qi, W. H.; Wang, M. P. Size and Shape Dependent Lattice Parameters of Metallic Nanoparticles. *J. Nanopart. Res.* **2005**, *7*, 51−57.
(18) Diehm, P. M.; Ágoston, P.; Albe, K. Size-Dependent Lattice Expansion in Nanoparticles: Reality or Anomaly? *ChemPhysChem* **2012**, *13*, 2443−2454.
(19) Prabhu, Y. T.; Rao, K. V.; Kumar, V. S.; Kumari, B. S. X-Ray Analysis By Williamson-Hall and Size-Strain Plot Methods of Zno Nanoparticles with Fuel Variation. *World J. Nano Sci. Eng.* **2014**, *4*, 21−28.
(20) Randrianantoandro, N.; Mercier, A. M.; Hervieu, M.; Grenèche, J. M. Direct Phase Transformation from Hematite to Maghemite During High Energy Ball Milling. *Mater. Lett.* **2001**, *47*, 150−158.
(21) Li, W.; Liang, X.; An, P.; Feng, X.; Tan, W.; Qiu, G.; Yin, H.; Liu, F. Mechanisms on The Morphology Variation of Hematite Crystals by Al Substitution: The Modification of Fe and O Reticular Densities. *Sci. Rep.* **2016**, *6*, 35960.
(22) Ayyub, P.; Multani, M.; Barma, M.; Palkar, V. R.; Vijayaraghavan, R. Size-Induced Structural Phase Transitions and Hyperfine Properties of Microcrystalline $Fe_2O_3$. *J. Phys. C: Solid State Phys.* **1988**, *21*, 2229−2245.
(23) Lu, L.; Li, L.; Wang, X.; Li, G. Understanding of The Finite Size Effects on Lattice Vibrations and Electronic Transitions of Nano $\alpha$-$Fe_2O_3$. *J. Phys. Chem. B* **2005**, *109*, 17151−17156.
(24) Tajiri, T.; Saisho, S.; Mito, M.; Deguchi, H.; Konishi, K.; Kohno, A. Size Dependence of Crystal Structure and Magnetic Properties of Nio Nanoparticles in Mesoporous Silica. *J. Phys. Chem. C* **2015**, *119*, 1194−1200.
(25) Lee, J. D. *Concise Inorganic Chemistry*; Chapman & Hall: London, 1991.
(26) Stavitski, E.; De Groot, F. M. F. The CTM4XAS Program for EELS and XAS Spectral Shape Analysis of Transition Metal L Edges. *Micron* **2010**, *41*, 687−694.
(27) Miedema, P. S.; Borgatti, F.; Offi, F.; Panaccione, G.; De Groot, F. M. F. Iron 1s X-Ray Photoemission of $Fe_2O_3$. *J. Electron Spectrosc. Relat. Phenom.* **2015**, *203*, 8−13.
(28) De Groot, F. M. F.; Grioni, M.; Fuggle, J. C.; Ghijsen, J.; Sawatzky, G. A.; Petersen, H. Oxygen 1s X-Ray-Absorption Edges of Transition-Metal Oxides. *Phys. Rev. B: Condens. Matter Mater. Phys.* **1989**, *40*, 5715−5723.
(29) Schedel-Niedrig, T.; Weiss, W.; Schlögl, R. Electronic Structure of Ultrathin Ordered Iron Oxide Films Grown Onto Pt(111). *Phys. Rev. B: Condens. Matter Mater. Phys.* **1995**, *52*, 17449−17460.
(30) Cramer, S. P.; DeGroot, F. M. F.; Ma, Y.; Chen, C. T.; Sette, F.; Kipke, C. A.; Eichhorn, D. M.; Chan, M. K.; Armstrong, W. H. Ligand Field Strengths and Oxidation States from Manganese L-Edge Spectroscopy. *J. Am. Chem. Soc.* **1991**, *113*, 7937−7940.
(31) Van Schooneveld, M. M.; Kurian, R.; Juhin, A.; Zhou, K.; Schlappa, J.; Strocov, V. N.; Schmitt, T.; De Groot, F. M. F. Electronic Structure of CoO Nanocrystals and A Single Crystal Probed by Resonant X-Ray Emission Spectroscopy. *J. Phys. Chem. C* **2012**, *116*, 15218−15230.
(32) Fujii, T.; Alders, D.; Voogt, F. C.; Hibma, T.; Thole, B. T.; Sawatzky, G. A. In Situ RHEED and XPS Studies of Epitaxial Thin $\alpha$-$Fe_2O_3$ (0001) Films on Sapphire. *Surf. Sci.* **1996**, *366*, 579−586.
(33) Ma, J.; Lian, J.; Duan, X.; Liu, X.; Zheng, W. $\alpha$-$Fe_2O_3$: Hydrothermal Synthesis, Magnetic and Electrochemical Properties. *J. Phys. Chem. C* **2010**, *114*, 10671−10676.
(34) Muruganandham, M.; Amutha, R.; Sathish, M.; Singh, T. S.; Suri, R. P. S.; Sillanpää, M. Facile Fabrication of Hierarchical $\alpha$-$Fe_2O_3$: Self-Assembly and Its Magnetic and Electrochemical Properties. *J. Phys. Chem. C* **2011**, *115*, 18164−18173.
(35) Onari, S.; Arai, T.; Kudo, K. Infrared Lattice Vibrations and Dielectric Dispersion in$\alpha$-$Fe_2O_3$. *Phys. Rev. B: Solid State* **1977**, *16*, 1717−1721.
(36) Chamritski, I.; Burns, G. Infrared- and Raman-Active Phonons of Magnetite, Maghemite, and Hematite: A Computer Simulation and Spectroscopic Study. *J. Phys. Chem. B* **2005**, *109*, 4965−4968.
(37) O'Neal, K. R.; Patete, J. M.; Chen, P.; Holinsworth, B. S.; Smith, J. M.; Lee, N.; Cheong, S.-W.; Wong, S. S.; Marques, C.; Aronson, M. C.; et al. Size-dependent Vibronic Coupling in $\alpha$-$Fe_2O_3$. *J. Chem. Phys.* **2014**, *141*, 2012−2017.
(38) Zou, B.; Huang, W.; Han, M. Y.; Li, S. F. Y.; Wu, X.; Zhang, Y.; Zhang, J.; Pengfei, W.; Wang, R. Anomalous Optical Properties and Electron-Phonon Coupling Enhancement in $Fe_2O_3$ Nanoparticles Coated with a Layer of Stearates. *J. Phys. Chem. Solids* **1997**, *58*, 1315−1320.
(39) Bersani, D.; Lottici, P. P.; Montenero, A. Micro-Raman Investigation of Iron Oxide Films and Powders Produced by Sol-Gel Synthesis. *J. Raman Spectrosc.* **1999**, *30*, 355−360.
(40) Legodi, M. A.; De Waal, D. The Preparation of Magnetite, Goethite, Hematite and Maghemite of Pigment Quality from Mill Scale Iron Waste. *Dyes Pigm.* **2007**, *74*, 161−168.
(41) De Faria, D. L. A.; Silva, S. V.; De Oliveira, M. T. Raman Microspectroscopy of Some Iron Oxides and Oxyhydroxides. *J. Raman Spectrosc.* **1997**, *28*, 873−878.
(42) Brahma, P.; Dutta, S.; Pal, M.; Chakravorty, D. Magnetic and Transport Properties of Nanostructured Ferric Oxide Produced by Mechanical Attrition. *J. Appl. Phys.* **2006**, *100*, 044302.
(43) Mott, N. F. Conduction in Glasses Containing Transition Metal Ions. *J. Non-Cryst. Solids* **1968**, *1*, 1−17.
(44) Mott, N. F.; Davis, E. A. *Electronic Processes in Non-crystalline Materials*; Clarendon Press: Oxford, 1971.
(45) Austin, I. G.; Mott, N. F. Polarons in Crystalline and Non-Crystalline Materials. *Adv. Phys.* **1969**, *18*, 41−102.
(46) Millis, A. J.; Shraiman, B. I.; Mueller, R. Dynamic Jahn-Teller Effect and Colossal Magnetoresistance in $La_{1-x}Sr_xMnO3$. *Phys. Rev. Lett.* **1996**, *77*, 175−178.
(47) Morin, F. J. Electrical Properties of $\alpha$-$Fe_2O_3$. *Phys. Rev.* **1954**, *93*, 1195−1199.
(48) Leland, J. K.; Bard, A. J. Photochemistry of Colloidal Semiconducting Iron Oxide Polymorphs. *J. Phys. Chem.* **1987**, *91*, 5076−5083.
(49) Dghough, L.L.; Elidrissi, B.; Bernède, C.; Addou, M.; Alaoui Lamrani, M.; Regragui, M.; Erguig, H. Physico-Chemical, Optical and Electrochemical Properties of Iron Oxide Thin Films Prepared by Spray Pyrolysis. *Appl. Surf. Sci.* **2006**, *253*, 1823−1829.
(50) Gilbert, B.; Frandsen, C.; Maxey, E. R.; Sherman, D. M. Band-Gap Measurements of Bulk and Nanoscale Hematite by Soft X-Ray Spectroscopy. *Phys. Rev. B: Condens. Matter Mater. Phys.* **2009**, *79*, 035108.


DOI: 10.1021/acs.jpcc.8b00550
J. Phys. Chem. C 2018, 122, 9292−9301

(51) Fondell, M.; Jacobsson, T. J.; Boman, M.; Edvinsson, T. Optical Quantum Confinement in Low Dimensional Hematite. *J. Mater. Chem. A* **2014**, *2*, 3352−3363.
(52) Vayssieres, L.; Sathe, C.; Butorin, S. M.; Shuh, D. K.; Nordgren, J.; Guo, J. One-Dimensional Quantum-Confinement Effect in $\alpha$-$Fe_2O_3$ Ultrafine Nanorod Arrays. *Adv. Mater.* **2005**, *17*, 2320−2323.



DOI: 10.1021/acs.jpcc.8b00550
*J. Phys. Chem. C* 2018, 122, 9292−9301